On Thermally Forced Circulations over Heated Terrain

DANIEL J. KIRSHBAUM

Department of Atmospheric and Oceanic Sciences, McGill University, Montreal, Quebec, Canada

ABSTRACT

A combination of analytical and numerical models is used to gain insight into the dynamics of thermally forced circulations over diurnally heated terrain. Solutions are obtained for two-layer flows (representing the boundary layer and the overlying free troposphere) over an isolated mountainlike heat source. A scaling based on the linearized Boussinesq system of equations is developed to quantify the strength of thermally forced updrafts and to identify three flow regimes, each with distinct dynamics and parameter sensitivities. This scaling closely matches corresponding numerical simulations in two of these regimes: the first characterized by a weakly stable boundary layer and significant background winds and the second by a strongly stable boundary layer. In the third regime, characterized by weak winds and weak boundary layer stability, this scaling is outperformed by a fundamentally different scaling based on thermodynamic heat engines. Within this regime, the inability of wind ventilation or static stability to diminish the buoyancy over the heat source leads to intense updrafts that are controlled by nonlinear dynamics. These nonlinearities create a positive feedback loop between the thermal forcing and vorticity that rapidly strengthens the circulation and contracts its central updraft into a narrow core. As the circulation intensifies under daytime heating, the warmest surface-based air is ventilated into the upper boundary layer, where it spreads laterally to occupy a broader area and, ultimately, restrain the circulation strength. The success demonstrated herein of simple theoretical models at predicting key aspects of thermally forced circulations offers hope for improved parameterization of related processes (e.g., convection initiation and aerosol venting) in large-scale models.

1. Introduction

Under daytime insolation, elevated terrain warms faster than the surrounding atmosphere at the same vertical level. The associated horizontal buoyancy gradients drive thermal circulations, which may be enhanced or diminished by variations in sensible heat fluxes over the higher terrain. These circulations are responsible for important meteorological phenomena like the initiation of deep convection and venting of aerosols out of the boundary layer (e.g., Banta 1990). Even over broad mountain ranges, the updraft branches of these circulations may collapse into intense finescale circulations (e.g., Barthlott et al. 2011), rendering them difficult to capture in weather and climate models with grid spacings of a few kilometers or larger. Thus a strong conceptual understanding of their dynamics is required

for their effects to be adequately represented in these models.

Although theoretical studies of thermally forced anabatic (upslope) flow along an infinite slope are numerous (e.g., Defant 1952; Haiden 2003), they do not address localized convective updrafts over the mountain crest that form owing to the convergence of airflow from opposite sides. These can be represented using linear theory, provided that the circulations are sufficiently weak that the linear approximation is valid. Reisner and Smolarkiewicz (1994) and Crook and Tucker (2005, hereafter CT05) used linear theory to study the impact of elevated heating on upstream blocking and mountain waves, respectively. However, these studies only considered steady-state solutions in a uniform atmosphere, which is a poor representation of real diurnal circulations that vary over finite time scales and form within more complex vertically layered flows. An alternative approach, which retains the steady-state assumption but relaxes the linear assumption, is the thermodynamic heat-engine framework (Renno and Ingersoll 1996). This was used by Souza et al. (2000) and Tian and Parker

Corresponding author address: Daniel Kirshbaum, Department of Atmospheric and Oceanic Sciences, 805 Sherbrooke St. W, Montreal QC H3A 0B9, Canada.
E-mail: daniel.kirshbaum@mcgill.ca

(2003) to relate thermally forced circulations over complex terrain—in well-mixed boundary layers with weak background winds—to the associated elevated thermal perturbation. Although this provided accurate diagnoses of updraft strength in nonlinear flows, its utility for prognosing updraft magnitude or for addressing more complex flows (e.g., stably stratified cross-barrier flows with significant background wind speeds) has yet to be demonstrated.

Uniform heating over elevated terrain produces a dynamically similar response to differential heating over flat terrain. Thus, studies of the sea–land breeze and other topographically forced circulations (e.g., flows induced by land surface heterogeneity) are relevant to the terrain-heating problem. Although a thorough review of this large body of literature is outside of the scope of this study, a handful of theoretical studies on the sea–land breeze are particularly relevant. Rotunno (1983) considered linear theory of the sea–land breeze in a uniformly stratified atmosphere with zero background wind, focusing on the latitudinal variation of the flow response and the phasing between the surface heating function and the thermal circulation. Qian et al. (2009) and Jiang (2012a) extended this linear theory by including, respectively, a background wind and irregularities in coastline shape. Although these studies have advanced conceptual understanding, they did not address the impact of boundary layer stability or the role of nonlinear dynamics on the dynamical response, both of which may be critically important in real flows. The linear theory of Jiang (2012b) did consider multilayer stability profiles, but it was applied to the problem of offshore gravity wave propagation rather than the strength of boundary layer circulations.

The objective of this study is to gain conceptual insight into the dynamics and sensitivities of topographically forced thermal circulations. To this end, a combination of linear theory, heat-engine theory, and nonlinear numerical simulations is used. The linear model fundamentally differs from previous linear studies of the terrain-heating problem (Reisner and Smolarkiewicz 1994; CT05) in that its consideration of both time variability and multilayer stability profiles admits important effects that were previously neglected. Although this theory is oversimplified and restricted by the small-amplitude approximation, its capacity to provide a predictive dynamical solution and to represent complex background flows and terrain shapes makes it a logical starting point for such an investigation. From the linearized equations a new scaling for updraft velocity is derived, the results from which are compared to nonlinear solutions and predictions from the heat-engine theory. Comparisons are provided for a wide range of

boundary layer stabilities, background wind speeds, and terrain geometries, with a focus on narrower hills (widths of 1–20 km) that are poorly resolved in numerical forecast models and for which the Coriolis force may be neglected. This scaling is also applied to determine the validity of the linear approximation and to identify three flow regimes with distinct dynamical responses and parameter sensitivities. Finally, the numerical simulations are analyzed to gain insight into the dynamical mechanisms of the nonlinear regime.

2. Methodology

a. Linear model

As in previous studies (e.g., Robinson et al. 2008) a semianalytical solution is obtained to the dry, linearized, two-dimensional (2D) Boussinesq system of equations. Although 2D is a major limitation that limits the real-world applicability of these results, it enables straightforward physical interpretations and thus provides a basis for understanding more complicated flows. The Coriolis force is neglected and the background flow is assumed to be steady, which renders this analysis most applicable to synoptically quiescent tropical or high-Rossby-number midlatitude flows. We begin by presenting a form of the dry, nonlinear, 2D Boussinesq system that represents the basis for all linear and nonlinear analysis to follow:

$$\frac{\partial \mathbf{v}}{\partial t} + (\mathbf{v} \cdot \nabla)\mathbf{v} = -\nabla P + b\hat{k} - \alpha \mathbf{v}', \tag{1}$$

$$\frac{\partial b}{\partial t} + (\mathbf{v} \cdot \nabla)b = -N^2 w + Q - \alpha b, \tag{2}$$

$$\nabla \cdot \mathbf{v} = 0, \tag{3}$$

where $\mathbf{v} = \overline{\mathbf{v}} + \mathbf{v}'$ is the total wind velocity, decomposed into a mean $[\overline{\mathbf{v}} = (\overline{U}, 0)$, where $\overline{U}$ is a zonal background wind] and perturbation $[\mathbf{v}' = (u, w)]$ component. In addition, $P = p/\rho_0$ is the density-normalized pressure perturbation (relative to the hydrostatically balanced basic state) and p and ρ_0 are the pressure perturbation and reference density, $b = g\theta'/\theta_0$ is the buoyancy and θ' and θ_0 are the perturbation and reference potential temperature, Q is a prescribed heating function, and N is the Brunt–Väisälä frequency. The time-dependent variables are u, w, b, and P. To represent dissipation, Rayleigh damping terms are added to the right-hand sides of each prognostic equation, all with the coefficient $\alpha = 2 \times 10^{-5}$ s^{-1}, which is similar to that inferred experimentally and used in previous linear studies (e.g., Stevens et al. 2002; Jiang 2012a). By expanding (1) and

removing all products of perturbation terms, we obtain the linearized equations for a given layer (where the layer number is denoted by the subscript i):

$$\frac{\partial u_i}{\partial t} + \overline{U}\frac{\partial u_i}{\partial x} = -\frac{\partial P_i}{\partial x} - \alpha u_i, \tag{4}$$

$$\frac{\partial w_i}{\partial t} + \overline{U}\frac{\partial w_i}{\partial x} = -\frac{\partial P_i}{\partial z} + b_i - \alpha w_i, \tag{5}$$

$$\frac{\partial b_i}{\partial t} + \overline{U}\frac{\partial b_i}{\partial x} = -N_i^2 w_i + Q_i - \alpha b_i, \tag{6}$$

$$\frac{\partial u_i}{\partial x} + \frac{\partial w_i}{\partial z} = 0. \tag{7}$$

The diurnally varying surface-based heat source Q is based on CT05, who considered a steady, exponentially decaying heating function of the form

$$Q = Q_0 e^{-(z-h)/D}, \tag{8}$$

where $h = h_m e^{-[(x-x_c)/a_m]^2}$ is a Gaussian terrain profile with a peak of h_m, a half-width of a_m, and a centerpoint of x_c; D is an e-folding heating decay scale; and $Q_0 = g\dot{T}/T_0$, where $\dot{T}$ is a heating rate (K s^{-1}) and T_0 is a reference temperature. Because the heating function is horizontally invariant over flat terrain, the only source of baroclinicity is variations in terrain height. To the accuracy of the linear approximation, the differential heating owing to elevated terrain is given by

$$Q(x, z, t) = q(x, t)e^{-z/D} = Q_0 \frac{h(x)}{D} e^{i\Omega t} e^{-z/D}, \tag{9}$$

where $\Omega = 2\pi$ day^{-1} is the earth's angular speed. This expression, which is henceforth used in (6), is identical to that used by CT05 except for its inclusion of diurnal variability (the time-varying exponential).

Although this formulation contains important features that were previously neglected, it still fails to capture many real-world complexities. First, it does not take into account diurnal changes in boundary layer stability—it only isolates the dynamical impacts of diurnal heating and cooling within a steady background flow. Similarly, the assumption of an exponential heating function (9) with a fixed vertical structure differs from reality, where the effective heating depth shrinks in the stable nocturnal boundary layer. Despite these simplifications, this formulation allows for an attractively straightforward analysis that, as will be seen, does offer useful insights into more complex flows.

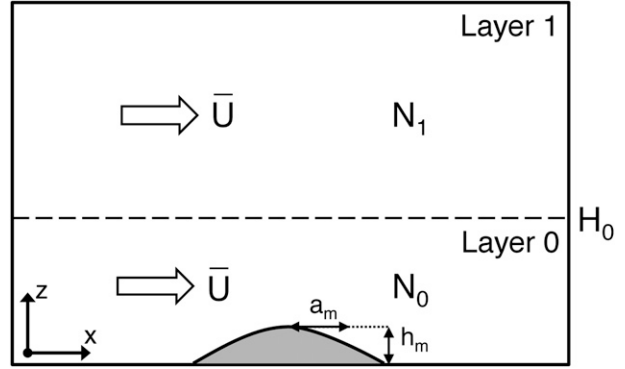With some arithmetic, the above system of equations may be combined into a single partial differential equation for w_i:

FIG. 1. Schematic diagram of two-layer model. All symbols are defined in the text.

$$\left(\frac{\partial}{\partial t} + \overline{U}\frac{\partial}{\partial x} + \alpha\right)^2 \left(\frac{\partial^2 w_i}{\partial x^2} + \frac{\partial^2 w_i}{\partial z^2}\right) + N_i^2 \frac{\partial^2 w_i}{\partial x^2} = \frac{\partial^2 Q_i}{\partial x^2}. \tag{10}$$

Applying the Fourier transform in the x and time dimensions, w in (10) may be represented as $w(x, z, t) = \text{Re}[\iint \hat{w}(k, z, \omega)e^{-i(kx-\omega t)}\, dk\, d\omega]$, where k is the horizontal wavenumber and ω the angular frequency. Because only the diurnal temporal mode is considered (i.e., $\omega = \Omega$), this may be simplified to $w(x, z, t) = \text{Re}[e^{i\Omega t}\int \hat{w}(k, z)e^{-ikx}\, dk]$ (e.g., Jiang 2012a). Adopting this representation, (10) may be written as an ordinary differential equation

$$\frac{\partial^2 \hat{w}_i}{\partial z^2} + m_i^2 \hat{w}_i = \frac{k^2}{\sigma^2}\hat{Q}, \tag{11}$$

where $\sigma = \Omega - Uk - i\alpha$ and $m_i^2 = k^2(N_i^2 - \sigma^2)/\sigma^2$. We solve (11) for a two-layer atmosphere (layers 0 and 1) with stabilities N_0 and N_1, separated by an interface at $z = H_0$ (shown schematically in Fig. 1). This configuration can accommodate a uniform stability profile as in previous studies (e.g., CT05) or a more realistic weakly stratified boundary layer beneath a stable free troposphere [as in Jiang (2012b)].

The linear model is solved by applying four boundary conditions: a free-slip lower surface, an upper radiation condition, and matching of displacement and pressure at $z = H_0$ (see appendix for details). It is represented on a discretized x-periodic domain with a length of $L_x = 400$ km and a grid spacing of $\Delta x_{\text{lin}} = 0.2a_m$. These values of domain length and horizontal resolution are large enough to ensure numerical robustness yet small enough to allow for efficient solutions. Because the Fourier transform is not applied in the vertical, the solution does not depend on the vertical grid settings. Thus the domain depth L_z is set to be just high enough to contain

the dynamics of interest, and the vertical grid spacing is $\Delta z_{lin} = 50$ m to adequately resolve the low-level flow.

b. The heat-engine framework

Renno and Ingersoll (1996) and Souza et al. (2000) developed a theory for thermally driven topographic circulations based on an analogy with thermodynamic heat engines, which was refined and applied to the mountain heating problem by Tian and Parker (2003). This theory is briefly reviewed here and applied to the flows under consideration in subsequent sections. The approach integrates Bernoulli's equation and the first law of thermodynamics around the closed loop of a steady-state convective circulation. This allows the strength of a convective updraft W_t to be related to the total convective available potential energy available for mechanical work (TCAPE) by the following expression:

$$W_t = \left(\frac{\text{TCAPE}}{\mu}\right)^{1/2}, \qquad (12)$$

where μ is a dimensionless coefficient of mechanical dissipation. In a dry convective boundary layer, TCAPE $\approx \eta c_p \Delta T$, where η is the thermodynamic efficiency of the heat engine, c_p is the specific heat of dry air at constant pressure, and ΔT is the mean horizontal temperature difference between the updrafts and downdrafts, or the "nonadiabatic" temperature difference between the heated terrain and the surrounding plain. In our experiments, the maximum ΔT may be estimated by integrating the positive phase of the surface heating function [from 0600 to 1800 local time (LT), or $t = -\pi/2\Omega$ to $t = \pi/2\Omega$]:

$$\Delta T \approx \int_{-\pi/2\Omega}^{\pi/2\Omega} \dot{T} \cos(\Omega t)\, dt = \frac{2\dot{T}}{\Omega}. \qquad (13)$$

Assuming that the system acquires its heat from the surface and dissipates it at the top of the convective boundary layer, the thermodynamic efficiency may be written

$$\eta = \frac{T_h - T_c}{T_h} \approx \frac{gH_0}{c_p T_0} \qquad (14)$$

(Souza et al. 2000), where T_h is the temperature of the hot reservoir (the heated surface) and T_c is the temperature of the cold reservoir (the boundary layer top). To obtain μ we use the formulation from Tian and Parker (2003), which assumes that scale of the dominant convective circulation is dictated by the geometry of the surface heat source and the boundary layer depth:

$$\mu \approx 8\left(\frac{H_0 + a_m}{H_0}\right). \qquad (15)$$

Substituting (13)–(15) into (12), we obtain

$$W_t = H_0 \left[\frac{g\dot{T}}{4T_0\Omega(H_0 + a_m)}\right]^{1/2}. \qquad (16)$$

Because the terrain is idealized as a flat heat source, no provision is made for the adiabatic temperature difference between the mountain base and peak, but it may be easily incorporated if needed (Tian and Parker 2003). Note that although the diurnally varying situations considered herein are obviously not in steady state, this theory is still reasonable if the time scale for an air parcel to loop through the circulation is much shorter than the diurnal time scale. This condition is only satisfied in the more strongly forced cases with more vigorous convective circulations; thus, as will be seen, the theory tends to poorly represent weakly forced cases. Note also that because this derivation assumes a closed circulation in a convective boundary layer, we only apply it to cases with $\overline{U} = N_0 = 0$.

c. Idealized numerical simulations

To critically assess the validity of the linear approximation and to extend our examination to the nonlinear regime, we perform idealized numerical simulations with the Bryan cloud model (cm1), version 14 (Bryan and Fritsch 2002). This model solves the primitive moist atmospheric equations using a split time step procedure to maintain stability of acoustic modes. On the large time step, time integration is performed with a third-order Runge–Kutta scheme. Ten small time steps are performed for each large time step. Horizontal (vertical) advection uses a centered sixth-order scheme (a fifth-order scheme with implicit diffusion). Because no implicit diffusion is applied in the horizontal, explicit sixth-order horizontal diffusion is added to minimize spurious grid-scale waves. The domain dimensions are $L_x = 400$ km and $L_z = 12$ km and the grid resolution is $\Delta x_{sim} = 500$ m and $\Delta z_{sim} = 100$ m. Boundary conditions are open in x and closed in z with a free-slip lower surface and a Rayleigh damper over the uppermost 4 km to absorb upward-propagating gravity waves. The only physical parameterization used in the simulations is a 1.5-order TKE-based subgrid-turbulence scheme. The runs are "dry" in that they contain no water vapor.

The simulations are performed in double precision to diminish the amplitude of numerical roundoff error, which can trigger instabilities in weakly unstable flows

like some of those considered here. Although turbulent eddies are physically realistic, they mask the thermal circulations of interest and thus cause the numerical and analytical solutions to grossly differ. By suppressing their growth and allowing model diffusion and/or subgrid turbulence to carry out the mixing, we may directly compare the two models on equal footing. The simulated circulations are thus best interpreted as time-averaged fields within a turbulent flow. However, their reliance on subgrid-scale (rather than resolved) turbulence and numerical diffusion may underestimate the degree of boundary layer mixing as well as the entrainment across the boundary layer top. Because both effects tend to weaken the horizontal buoyancy gradients that drive thermal circulations, the numerical solutions obtained herein may tend to overestimate the strength of these circulations.

Except for a single simulation that verifies the validity of the localized heating function in (9) for representing elevated heating, all experiments use flat terrain with this heating function. This is done for consistency with the linear model and because it isolates the thermal response to localized heating, which is the focus of this study, in the absence of any mechanical forcing. Another benefit of this approach is that the results are generalizable to any mechanism of differential surface heating (such as land surface heterogeneities).

The model initialization must be handled with some care to reasonably match the linear solutions. Because the linear flow dynamics are periodic in time and state-variable perturbations are always present over the flow volume, starting the model from rest (or with a uniform basic-state flow) imposes differences from the linear solution that persist indefinitely. To overcome this problem, the model was started from rest but the forcing was linearly increased from zero to its full amplitude over the first 24 h of integration, after which the simulation was integrated for an additional 48 h. By allowing the flow dynamics to develop gradually, the numerical-model solutions were able to fall into line with the corresponding linear solutions. All simulations are initialized at 0600 LT so that $t = \pi/2\Omega$ and $Q = 0$ in (9).

3. Scaling

a. Vertical velocity scale

We begin by estimating a characteristic magnitude of the thermally induced updraft velocity W_t. Although such a scaling is straightforward for a uniform atmosphere, it can become much more challenging in multilayer flows where the dynamics of a given layer are influenced by interactions with surrounding layers.

However, if one restricts consideration to two basic yet highly relevant situations—a uniformly stratified atmosphere ($N_0 = N_1$) and a neutrally stratified boundary layer overlaid by a stable free troposphere ($N_0 = 0$)—simple yet accurate scalings do become possible.

We begin by nondimensionalizing the state variables through the following assignments: $x \sim L\tilde{x}$, $z \sim H\tilde{z}$, $t \sim \Omega^{-1}\tilde{t}$, $w \sim W_t\tilde{w}$, $u \sim U\tilde{u}$, and $Q \sim (Q_0 h_m/D)\tilde{Q}$, where the variables with tilde symbols are nondimensional and of $\mathcal{O}(1)$. Substituting these relations into (10) and cancelling $\mathcal{O}(1)$ terms, we obtain the following expression for W_t:

$$W_t \sim \frac{Q_0 h_m D^{-1}}{(\Omega + \alpha + \overline{U}L^{-1})^2(1 + L^2/H^2) + N_0^2}. \quad (17)$$

Care is required in selecting the horizontal (L) and vertical (H) length scales. For the continuously stratified case ($N_0 = N_1$), the solution consists primarily of vertically propagating gravity waves. Following Rotunno (1983), the governing partial differential equation in (10) implies a natural aspect ratio of $L^2/H^2 \sim N_0^2/\sigma_L^2$. Since the prescribed horizontal (a_m) and vertical (D) forcing scales are unlikely to obey this relationship, only one of them can control the response. To identify the controlling scale, we first select $L^* = a_m$ and calculate the associated natural vertical scale ($H^* = a_m|\sigma_L|/N_0$). For $H^* > D$, we set $H = H^*$ to select the larger of the two relevant vertical scales, along with $L = a_m$. For $H^* < D$, we set $H = D$ and $L = DN_0/|\sigma_L|$ to again choose the larger scale and enforce the natural aspect ratio. In the latter case, because $|\sigma_L|$ is a function of L, the equation is implicit and an iterative procedure is required to solve for both $|\sigma_L|$ and L.

For the neutral boundary layer ($N_0 = 0$), the two-layer response does not conform to the natural aspect ratio of either layer alone. A mixed response develops in the vertical, with the dominant signal confined to the boundary layer and a weak extension into the stable free troposphere. An appropriate choice for the vertical scale is $H = H_0/2$, midway through the boundary layer where the strongest vertical motions are found. In the horizontal, where the circulation extent is dominated by the applied forcing scale, we set $L = a_m$.

b. Validity of linear theory

The linear approximation is only valid if the magnitudes of the linear terms in (4)–(7) are much larger than the (unwritten) nonlinear terms. To this end, we estimate the magnitude of the nonlinear advection terms in (5) and compare them to that of the dominant linear terms. This approach is valid under the weakly linear approximation, whereby the first-order perturbations

obtained from the linear solution may be used to estimate the second-order nonlinear terms. The nonlinear horizontal advection of w may be estimated as

$$u\frac{\partial w}{\partial x} \sim \frac{W_t^2}{H}, \tag{18}$$

where a scaling of (7) was used to estimate the magnitude of the perturbation u-wind. The specific choice of the nonlinear advection term in this equation (i.e., zonal advection versus vertical advection) is unimportant because both terms share the same characteristic magnitude. To estimate the magnitude of the linear terms, we first must identify which term on the left-hand side of (5) is dominant. This depends on $\Omega L/\overline{U}$; when $\Omega L/\overline{U} \ll 1$ the linear advection term dominates and when $\Omega L/\overline{U} \gg 1$ the time-tendency term dominates. This leads to two nonlinearity parameters (M_t) for the two cases:

$$M_t = \begin{cases} \dfrac{W_t L}{\overline{U} H} \ll 1: & \dfrac{\Omega L}{\overline{U}} \ll 1 \\[2ex] \dfrac{W_t}{\Omega H} \ll 1: & \dfrac{\Omega L}{\overline{U}} \gg 1 \end{cases}. \tag{19}$$

c. Flow regimes

Based on (6) and (17), three distinct flow regimes naturally emerge, the first being the "growth–decay"

TABLE 1. Regime classifications and scaled thermal and mechanical updraft velocities (W_t and W_m) from (17) for a few different combinations of $\overline{U}$ and N_0. In all cases $h_m = 100$ m, $a_m = 5$ km, $D = H_0 = 1$ km, and $Q_0 = g\dot{T}/T_0$, where $\dot{T} = 1$ K h^{-1} and $T_0 = 300$ K is a reference temperature. The linearity is determined by application of (19).

$\overline{U}$ (m s^{-1})	N_0 (s^{-1})	Regime	M_t	W_t (m s^{-1})	W_m (m s^{-1})	Name
0	0	GD	14	1.0	0	GD1
0	0.013	ST	0.06	0.005	0	ST1
2	0	VE	0.09	0.04	0.04	VE1
2	0.013	ST	0.002	0.005	0.04	ST2
5	0	VE	0.008	0.008	0.1	VE2
5	0.013	ST	0.0004	0.005	0.1	ST3

(GD) regime, where the heating term in (6) is balanced by the time-tendency and/or dissipation terms. One can show that this regime prevails when $\Omega + \alpha \gg [\overline{U}/L, N_0]$. The two other basic regimes are the "ventilation" (VE) regime ($\overline{U}/L \gg [\Omega + \alpha, N_0]$), where the heating is balanced by the linear advection term, and the "stratification" (ST) regime ($N_0 \gg [\Omega + \alpha, \overline{U}/L]$), where the heating is balanced by the stability term [the first on the right-hand side of (6)]. Based on these dominant balances, (17) can be simplified to give the following W_t estimates for each regime:

$$W_t \approx \begin{cases} \dfrac{Q_0 h_m H^2}{D(\Omega + \alpha)^2 L^2}: & \text{Growth–decay } (\Omega + \alpha \gg [\overline{U}/a_m, N_0]) \\[3ex] \dfrac{Q_0 h_m H^2}{D\overline{U}^2}: & \text{Ventilation } (\overline{U}/L \gg [\Omega + \alpha, N_0]) \\[3ex] \dfrac{Q_0 h_m}{D N_0^2}: & \text{Stratification } (N_0 \gg [\Omega + \alpha, \overline{U}/L]) \end{cases}, \tag{20}$$

where we have also assumed that $H/L \ll 1$. In all three regimes W_t depends directly on $Q_0 h_m/D$, which determines the low-level baroclinicity. It also increases with H^2 in the GD and VE regimes for two reasons: (i) based on the hydrostatic form of (6), the accumulation of buoyancy in a neutral layer gives rise to pressure perturbations (and hence horizontal wind perturbations U) that scale with H and (ii) from (7), $W_t \sim UH/L$, hence $W_t \sim H^2$. In the GD regime W_t is inversely dependent on $(\Omega + \alpha)^2$ and L^2, the former being the inverse time scale for perturbation growth and the latter controlling the horizontal buoyancy gradients that drive the circulation. In the VE regime, W_t depends inversely on $\overline{U}^2$, which causes downwind ventilation of heat and thus weakens the buoyancy anomalies over the heat source. Finally, in

the ST regime, W_t is inversely dependent on N_0^2, which controls the fluid resistance to vertical motion.

To provide a tangible comparison of the updraft magnitudes and linearity within these different flow regimes, Table 1 lists six different situations distinguished by their values of $\overline{U}$ and N_0 for a short ($h_m = 100$ m) and narrow ($a_m = 5$ km) mountain under moderate heating ($\dot{T} = 1$ K h^{-1}). Other parameters include $H_0 = 1$ km (for cases with $N_0 = 0$) and $T_0 = 300$ K. The regime classification, along with W_t and M_t, is provided for each case. Updrafts are the strongest, and the flow the most nonlinear, for a neutral boundary layer with $\overline{U} = 0$ (the GD regime). This is because neither stable ascent nor wind ventilation exists to diminish the growth of buoyancy over the heat source, so the response attains a large

amplitude. The updrafts are weaker and the flow more linear in the ST regime, owing to the effectiveness of stable ascent at balancing the imposed heating. The other linear term capable of effectively balancing the heating is horizontal advection by the background wind, which strongly reduces M_t in the VE regime. Thus the linear approximation is more valid in the ST and VE regimes than in the GD regime, where most real-world flows easily exceed the nonlinearity threshold. Nonetheless, the analysis in section 4 demonstrates that even in nonlinear cases, the linear theory is still useful for physically interpreting some (but not all) of the basic parameter sensitivities.

d. Mechanical forcing

In addition to inducing thermal circulations, mountains force mechanical ascent when the background cross-barrier winds are nonzero. For taller obstacles, strong interactions between mechanical and thermal forcing may occur, such as when flow splitting around a massif creates a decelerated wake region that gives rise to an amplified thermal circulation (e.g., Jury and Chiao 2011). However, because mechanical forcing is not a focus of this paper, a thorough analysis of such complex interactions is deferred to future work.

As a starting point, we restrict our analysis to the linear approximation—for which the thermal and mechanical responses formally decouple—and offer some preliminary insights into the relative strengths of the thermal and mechanical responses. The mechanical-lifting strength may be estimated from the free-slip lower boundary condition as $W_m \sim \overline{U} h_m / a_m$. Values of W_m are compared to W_t for the six cases in Table 1. The ratio of thermal to mechanical lifting is then given by

$$\frac{W_t}{W_m} = \frac{Q_0 a_m / \overline{U} D}{(\Omega + \alpha + \overline{U} L^{-1})^2 (1 + L^2 H^{-2}) + N_0^2}. \quad (21)$$

As before, one may simplify this ratio for the three regimes identified in section 3c:

$$\frac{W_t}{W_m} \approx \begin{cases} \dfrac{Q_0 a_m H^2}{D L^2 \overline{U} (\Omega + \alpha)^2}: & \text{Growth–decay } (\Omega + \alpha \gg [\overline{U}/L, N_0]) \\[2mm] \dfrac{Q_0 a_m H^2}{D \overline{U}^3}: & \text{Ventilation } (\overline{U}/L \gg [\Omega + \alpha, N_0]) \\[2mm] \dfrac{Q_0 a_m}{D \overline{U} N_0^2}: & \text{Stratification } (N_0 \gg [\Omega + \alpha, \overline{U}/L]) \end{cases} \quad (22)$$

This suggests that the thermal response tends to dominate when the cross-barrier winds and boundary layer stratification are weak, which is consistent with the numerical findings of Tian and Parker (2003), or when the heating rate and boundary layer depth are large. For the VE regime, the above scaling is identical to that derived by previous authors (Smith and Lin 1982; CT05). However, (22) reveals that those studies only addressed a fraction of the relevant parameter space.

4. Results

We first evaluate the approximation that the dynamical signature of elevated heating can be represented by a localized heat source over flat terrain. Figure 2 compares two simulations that are identical in all respects ($\overline{U} = 0$ m s^{-1}, $N_0 = 0$ s^{-1}, $N_1 = 0.013$ s^{-1}, $\dot{T} = 0.001$ K s^{-1}, $H_0 = D = 1$ km, $h_m = 10$ m, and $a_m = 5$ km) except for their application of surface heating. In the first case, a Gaussian terrain profile is used with the heating function $Q_{sfc} = Q_0 e^{(z-h)/D} e^{i\Omega t}$ applied uniformly over all x,

and in the second a flat terrain is used with the localized heating function (9). A low value of $\dot{T}$ is required to prevent the formation of turbulent eddies, which develop relatively easily in the former case. The w fields of both cases are very similar, with an updraft centered at $\tilde{x} = 0$ surrounded by two symmetric downdrafts. The central updraft is a bit shallower and wider, and the downdrafts stronger, in the uniform-heating case than in the localized heating case. Nonetheless, the reasonable agreement between the magnitudes and structures of these responses, which is largely maintained in simulations with much larger h_m (not shown), helps to justify the use of (9) for subsequent analysis.

a. Examples of linear solutions

Linear-model solutions for the "baseline" case of $h_m = 1$ m, $a_m = 5$ km, $\overline{U} = 0$ m s^{-1}, $N_0 = 0$ s^{-1}, $N_1 = 0.013$ s^{-1}, $H_0 = D = 1$ km, and $\dot{T} = 0.1$ K h^{-1} are shown in Fig. 3 alongside corresponding fields from the numerical solution. With its short terrain and weak forcing, this case falls well within the linear regime defined by
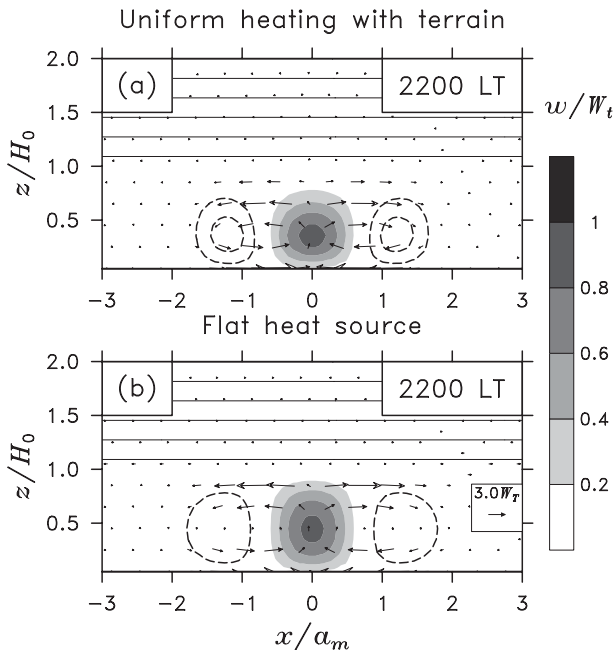
FIG. 2. Comparison of w fields for simulations with (a) a Gaussian terrain profile with horizontally uniform heating [see (8)] and (b) a flat terrain with a localized heat source [see (9)]. Both cases use the following environmental and terrain-related parameters: $\overline{U} = 0 \text{ m s}^{-1}$, $N_0 = 0 \text{ s}^{-1}$, $N_1 = 0.013 \text{ s}^{-1}$, $\dot{T} = 0.001 \text{ K s}^{-1}$, $H_0 = D = 1 \text{ km}$, $h_m = 10 \text{ m}$, and $a_m = 5 \text{ km}$. Filled grayscale contours denote positive vertical motion; dashed lines indicate negative vertical motion (using the same contour scale as in the color bar). Thin black contours are isentropes at a 1-K interval. The velocity reference scale in (b) also applies to (a).

(20). However, the linear and numerical model solutions are not identical. This is primarily due to the damping term in the linear system, which, at least in this case, is unrealistically large. Although one can reduce α to produce a nearly identical match between these two solutions, it would degrade the comparison for other cases, particularly those with stronger thermal forcing. Thus we hold α fixed and accept some modest disagreements between the two models.

The vertical-motion patterns in Fig. 3 generally differ from the steady-state solutions obtained by CT05 (e.g., their Fig. 4) that took the form of upstream-tilted vertically propagating gravity waves. These differences arise from our consideration of time variability, weak background winds, and a neutrally stratified boundary layer, all of which are common characteristics of thermally forced flows but were previously neglected. As in Fig. 2, the boundary layer response at 0000 LT is a solenoidal circulation with an updraft over the terrain centerpoint surrounded by two symmetric downdrafts. Strong horizontal convergence is apparent at the updraft bottom, with divergence at the boundary layer top. The peak

updraft speeds at that time are similar to the W_t estimates from (17).

Surprisingly, both models generate their strongest downdrafts at around noon and their strongest updrafts at around midnight, or about 12 h after these features normally develop in reality. As discussed by Rotunno (1983), this is due to the dominance of the time-tendency terms in (5) and (6), which together imply up to a 12-h lag between the Q maximum at 1200 LT and the peak kinematic response. This is seen by solving (5) and (6) for the idealized case of $P = \overline{U} = N_0 = \alpha = 0$ (i.e., the parcel approximation in a wind-free, neutral, inviscid flow), which gives $w = -Q/\Omega^2$. Hence, at least for this simple case, the phases of w and Q differ by 180°. In reality, the emergence of other terms in these equations, namely nonlinearities and turbulent dissipation, reduces the delay between the heating cycle and the kinematic response. This is reflected by Fig. 3, where the stronger effective dissipation in the linear model shifts the diurnal cycle of vertical motion forward by about 2 h. When α is increased to $1.0 \times 10^{-4} \text{ s}^{-1}$ the timing of the maximum updraft shifts forward all the way to 1400 LT (not shown).

Vertical velocity fields of linear solutions for the six cases from Table 1 are compared in Fig. 4, where the display times are chosen separately for each case to capture their mature responses to the daytime heating. A rich spectrum of dynamical responses arises depending on the choices of governing parameters. For zero wind, a vertically decaying plume of ascent develops with a maximum just above the surface in the stable case (ST1; Fig. 4b). This is surrounded by two vertically tilted downdraft beams, forming a gravity wave circulation that transports perturbation energy large distances from the heat source. This response differs from the solenoidal circulation in the neutral case (GD1; Fig. 4a), where the perturbations are stronger but more localized at the heat source. The differences in the timing of these responses relate to their different thermal inertia: whereas strong buoyancy anomalies are sustained for several hours after the heating ceases in the GD1 case, they are rapidly weakened by stable ascent in the ST1 case. When the stability term dominates over the time-tendency terms in (6), the vertical motion becomes in phase with the heating function and the strongest updraft occurs at noon.

For the neutral boundary layer, modest winds of $\overline{U} = 2 \text{ m s}^{-1}$ are sufficient to dramatically weaken the central updraft and displace it downwind (Fig. 4c). This is consistent with the cloud-resolving simulations of Kirshbaum (2011), where background winds of 1.5 m s^{-1} strongly weakened boundary layer updrafts and suppressed the initiation of deep convection. Stronger winds
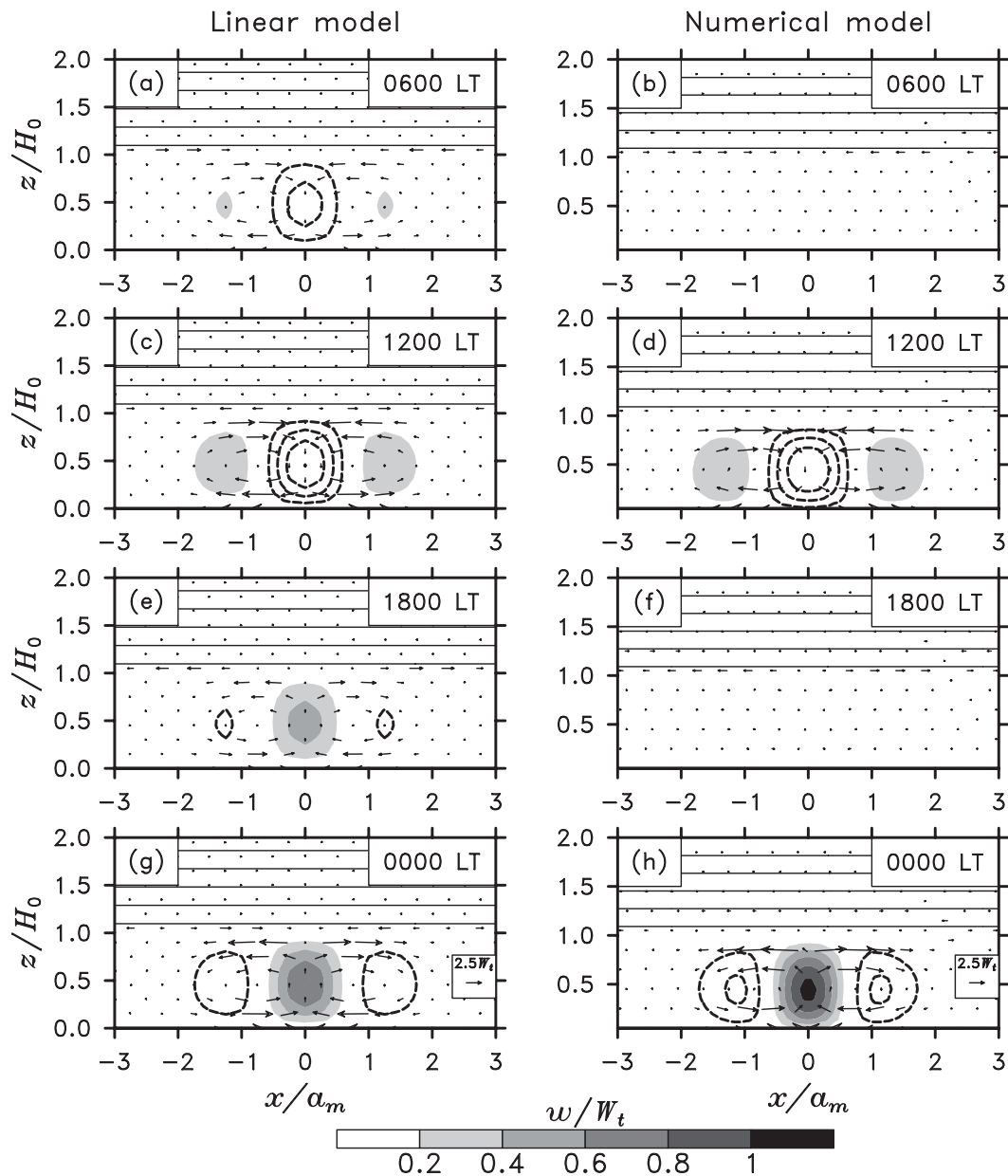
FIG. 3. Comparison of linear and numerical model solutions for the baseline case of $h_m = 1$ m, $a_m = 5$ km, $\overline{U} = 0$ m s^{-1}, $N_0 = 0$ s^{-1}, $H_0 = D = 1$ km, and $\dot{T} = 0.1$ K h^{-1}. Filled grayscale contours denote positive vertical motion; dashed lines denote negative vertical motion (using the same contour scale as in the color bar). Thin black contours are isentropes at a 1-K interval. The arrows show perturbation wind vectors. The velocity reference scales in (g) and (h) also apply to (a)–(f).

also cause the emergence of upstream-tilted, vertically propagating gravity waves, which become better defined for larger N_0 and $\overline{U}$ (Figs. 4c–f). These waves, which owe their existence to the interaction between ambient winds and a stationary heat source, are similar to those found in recent studies of sea-breeze dynamics (Qian et al. 2009; Jiang 2012b). As in CT05, the gravity wave response is characterized by low-level

descent upstream of the terrain, where the flow accelerates into the low pressure center, and ascent downwind. Because the exponential heating function extends into the stable troposphere, elevated waves form even in the neutral cases. However, these are not visible in the zero-wind case (Fig. 4a) because they are masked by the dominant boundary layer circulation. In all of the cases with nonzero winds, the thermal inertia is
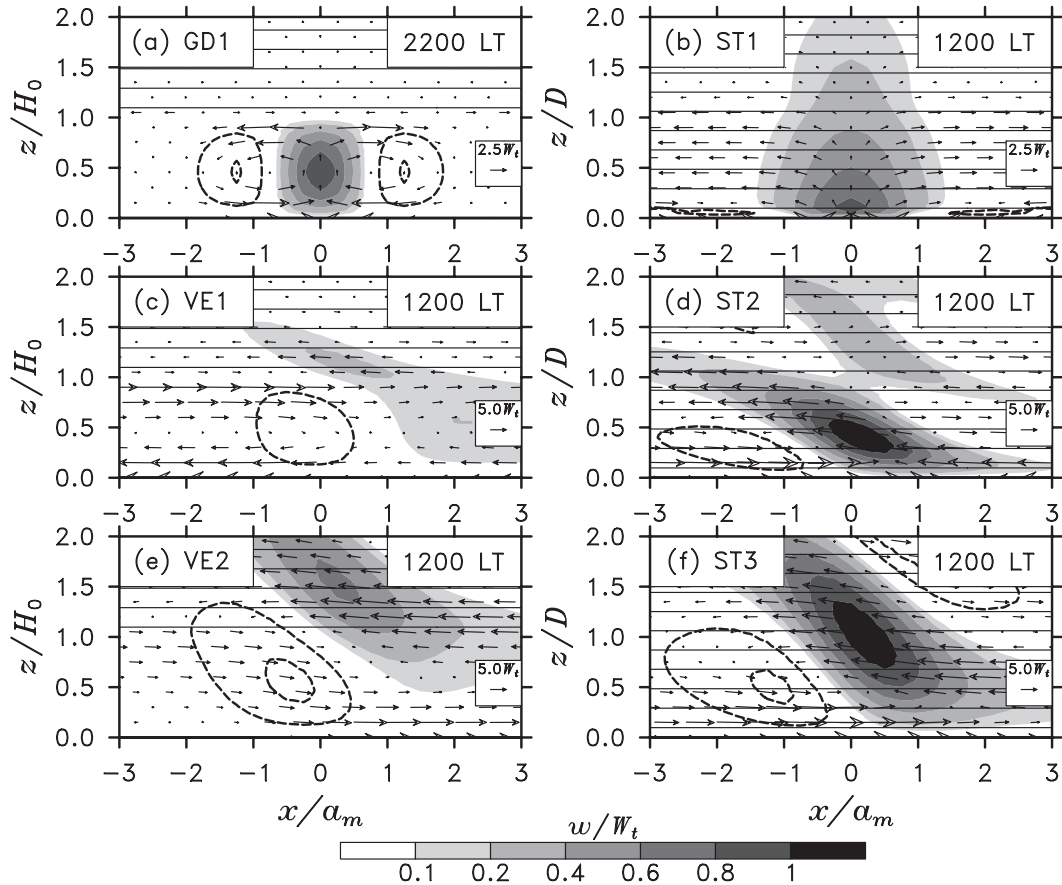
FIG. 4. As in Fig. 3, but for six different linear model solutions using the parameter settings in Table 1. For reference, the name of each case follows the convention in Table 1 and the time is shown in the upper-right corner. The times are chosen to capture the thermal response in a mature state over the 1200–0000 LT period. Thin black contours are isentropes at a 1-K interval.

diminished by horizontal advection and/or stable ascent/descent, so the diurnal updrafts are in phase with the heating cycle.

b. Parameter sensitivities

Experiments covering a broad range of parameter space are conducted to examine the environmental and terrain-related sensitivities of thermally forced updrafts. For all other parameters equal to the baseline case ($a_m =$ 5 km, $\overline{U} = 0$, $D = 1$ km, and $H_0 = 1$ km), Fig. 5 shows that the updraft magnitude depends nearly linearly on the terrain height h_m (for $\dot{T} = 0.1$ K h^{-1}) and the surface heating rate $\dot{T}$ (for $h_m = 1$ m), in agreement with (17). The W_t values from both the linear scaling and the numerical simulations are presented, the latter of which is taken as the maximum simulated w over the region $|x| \leq 5a_m$ and $z \leq 2H$ over the full diurnal cycle. Because of their close agreement with the linear scalings (and for the sake of clarity), the corresponding W_t values from the full linear solutions are omitted. Results are

compared for both a neutral boundary layer and a stable boundary layer with $N_0 = 0.013$ s^{-1}, indicating a dramatic (10^2–10^3-fold) enhancement of updraft velocity in the neutral case. A vertical dashed line is added to indicate the threshold values of $\dot{T}$ and h_m at which $M_t =$ 0.25 in (19), beyond which nonlinearities figure prominently in the numerical model solution. This threshold, which varies according to regime (see section 3c), is reached at much smaller values of h_m and $\dot{T}$ in the neutral case (for the stable boundary layer in Fig. 5a, this threshold falls outside the axis limits). The agreement between the simulated and scaled W_t is nearly exact in the linear regime and very good into the nonlinear regime.

Also shown in Fig. 5 are the corresponding W_t predictions from the heat-engine theory in (16), for the neutral cases only. These grossly overestimate W_t under weak forcing but closely match the simulations within the nonlinear regime. The poor performance in the linear regime is likely linked to the violation of the
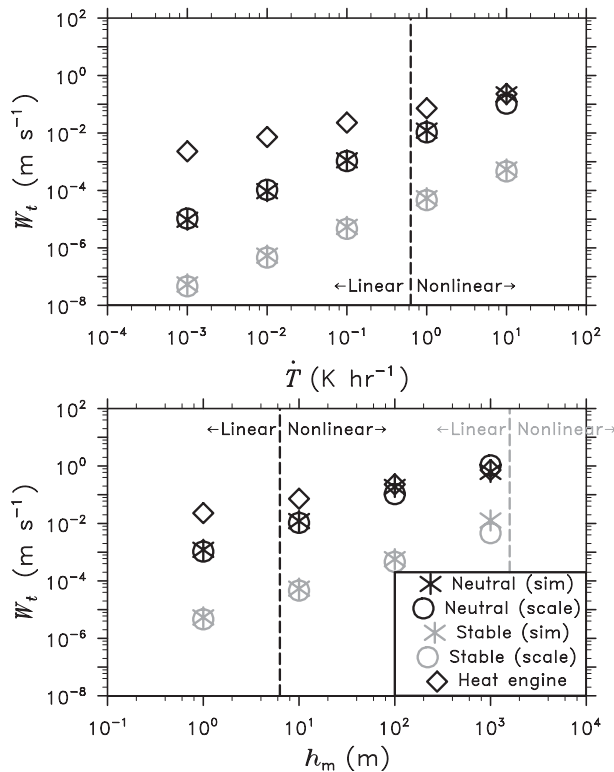
FIG. 5. Sensitivities of updraft velocity to (a) heating rate (for a fixed value of $h_m = 1$ m) and (b) mountain height (for a fixed value of $\dot{T} = 0.1$ K h^{-1}). Results for a neutral ($N_0 = 0$) and stable ($N_0 = 0.013$ s^{-1}) boundary layer are shown by black and gray markers, respectively. Nonlinearity thresholds of $M_t = 0.25$ are shown for by vertical dashed lines, adhering to the same color scale as the markers.

steady-state assumption in (16). With a characteristic updraft strength of $W_t \leq 0.1$ m s^{-1}, the time required for an air parcel to complete a full cycle through the convective circulation is over 12 h, which renders the steady-state assumption invalid. However, because meteorologically significant circulations usually exceed this strength, this overprediction in the linear regime is not a major concern.

The sensitivities of W_t to other governing parameters are shown in Fig. 6 for a weakly heated bump ($h_m = 1$ m, $\dot{T} = 0.1$ K h^{-1}) (left panels) and a strongly heated hill ($h_m = 100$ m, $\dot{T} = 1$ K h^{-1}) (right panels). With some exceptions, the updraft velocities in the neutral boundary layer are multiple orders of magnitude stronger than those in the stable boundary layer, which reinforces the strong sensitivity of W_t to N_0. The boundary layer stability also controls the sensitivity to background winds— whereas W_t sharply decreases with increasing $\overline{U}$ in the neutral case, it is insensitive to $\overline{U}$ for the stable case (Figs. 6a,b). The neutral boundary layer transitions from the GD into the VE regime for small values of $\overline{U}$,

causing W_t to become inversely proportional to $\overline{U}^2$ and thus decrease rapidly with increasing $\overline{U}$ in (20). By contrast, the stable cases lie uniformly within the ST regime, which from (20) implies no sensitivity to $\overline{U}$. One shortcoming of the linear scaling is that it overpredicts W_t in the neutral boundary layer for larger $\overline{U}$, likely because of its neglect of free-tropospheric gravity waves that extend downward into the boundary layer (e.g., Fig. 4e). Nonetheless, it still matches the simulations to within a factor of 2. Although the scaling performance worsens in the nonlinear regime (the neutral cases in Fig. 6b), it still captures the trend for W_t to decrease rapidly with increasing background winds. This suggests that the downwind advection of heat, a process reasonably well described by linear theory, is the principal mechanism for the rapid weakening of the updrafts for increasing $\overline{U}$.

Similarly, the neutral and stable boundary layers exhibit contrasting linear sensitivities to a_m: the former sharply decreases with increasing a_m but the latter is largely insensitive to it (Fig. 6c). In the neutral boundary layer, W_t is controlled by the amplitudes of horizontal buoyancy gradients, which, all else being equal, strengthen as the terrain narrows. By contrast, for a stable boundary layer the vertical motion is governed primarily by the stability and the heating-amplitude $Q_0 h_m/D$ [see (20)], which is invariant among these cases. Although the linear scaling performs extremely well in the linear regime, it performs poorly in the nonlinear regime where the simulations exhibit virtually no sensitivity to a_m (Fig. 6d). As will be discussed in section 5, this is due to nonlinear advection, which profoundly modifies the evolution of the convective circulation. Compared to the linear scaling, the heat-engine framework provides a much better estimate of W_t in the nonlinear regime.

The updrafts tend to strengthen with decreasing D and increasing H_0, both in the linear and nonlinear regimes (Figs. 6e–h). The linear scaling performs extremely well in the linear regime but, like the heat-engine model, it tends to overestimate W_t up to fourfold in the nonlinear regime. The linear scaling and heat-engine model show slightly different sensitivities to D and H_0, with the former overestimating the slope of the simulated trend and the latter underestimating it. The general overestimation of W_t by the heat-engine model may not be a flaw with the theory but the result of the assumption that ΔT equals the integrated surface-based heating in (13). This is surely an overestimate—advection and diffusion both diminish ΔT by transporting heat away from the terrain. Nonetheless, Figs. 5–6 illustrate that the theory generally performs well in the nonlinear GD regime. Thus it serves
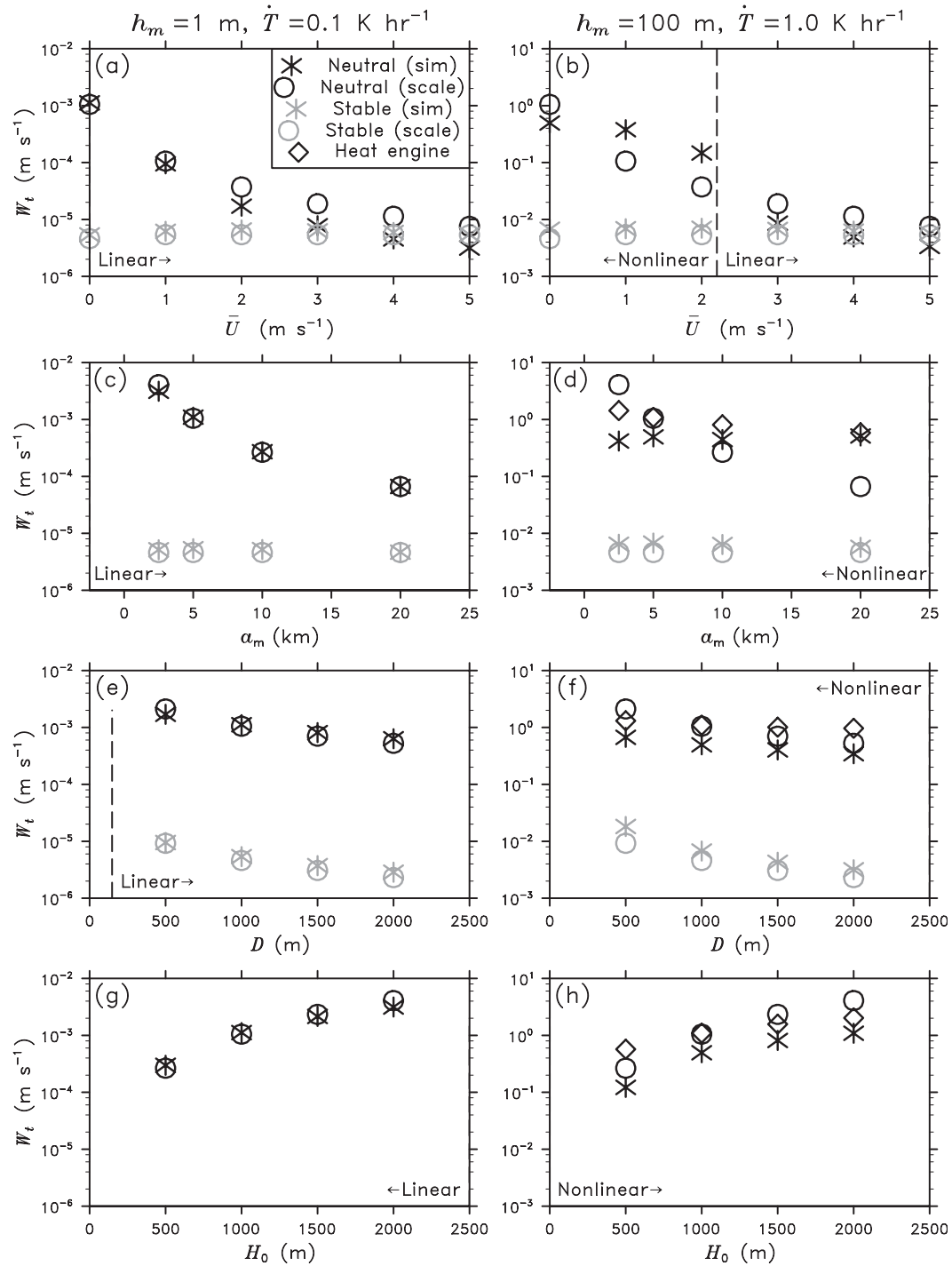
FIG. 6. Sensitivities of updraft velocity to (a),(b) background cross-barrier wind speed, (c),(d) terrain width, (e),(f) heating depth, and (g),(h) boundary layer depth, for a neutral ($N_0 = 0$, black) and stable ($N_0 = 0.013$ s^{-1}, gray) boundary layer. Left panels correspond to a short mountain and weak heating rate ($h_m = 1$ m and $\dot{T} = 0.1$ K h^{-1}), and right panels correspond to a taller hill and strong heating rate ($h_m = 100$ m and $\dot{T} = 1$ K h^{-1}). Nonlinearity thresholds of $M_t = 0.25$ are shown for the neutral cases by vertical dashed lines. These lines are not drawn for the stable cases, which all fall within the linear regime.
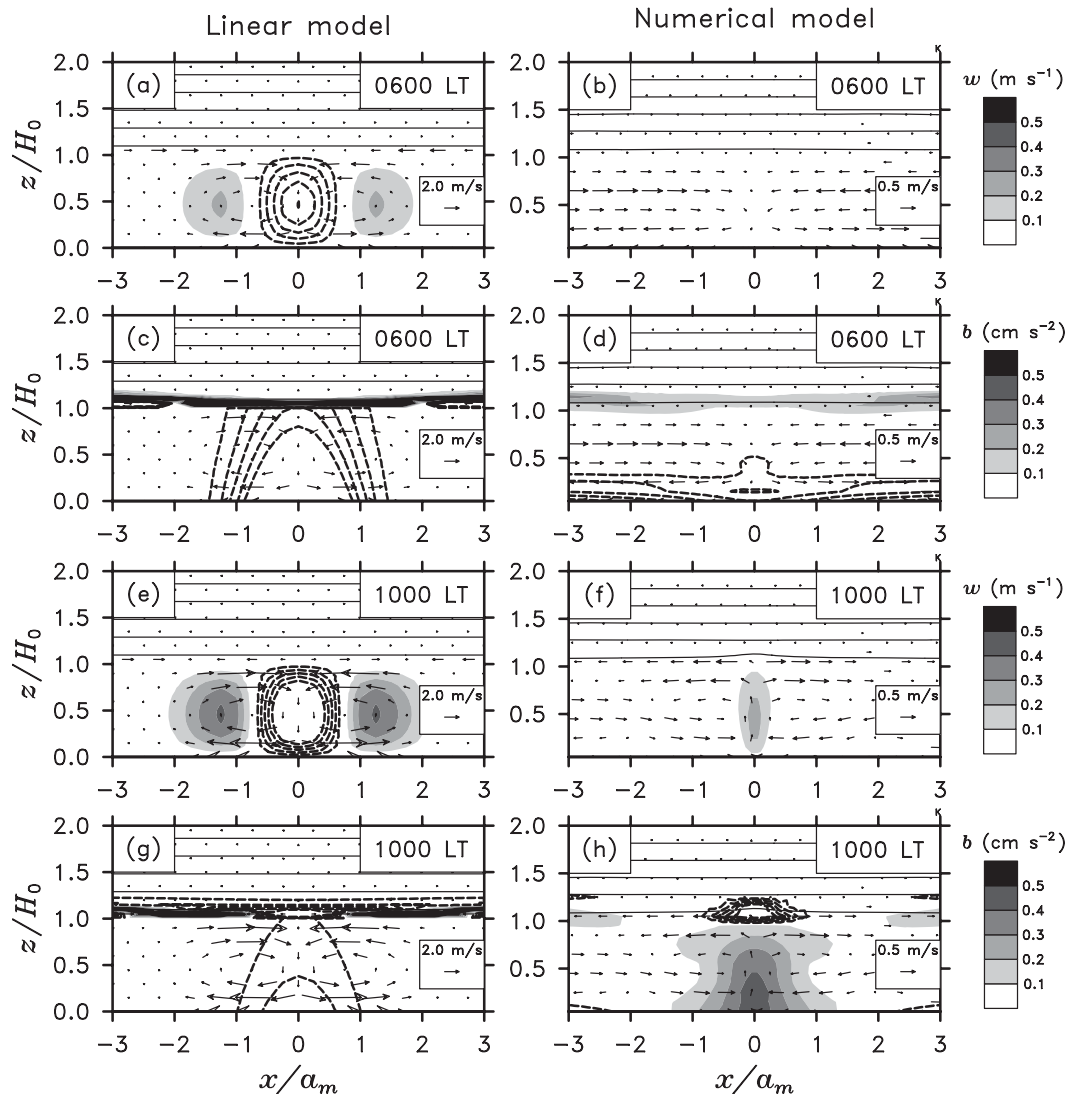
FIG. 7. Comparison of linear and numerical model solutions for the HM100-AM5 case. At 0600 LT, solutions for w are provided from the (a) linear and (b) numerical models, followed by b for the (c) linear and (d) numerical models. Similarly, 1000 LT solutions for w are provided from the (e) linear and (f) numerical models, followed by b from the (g) linear and (h) numerical models. Positive values are in filled grayscale contours and negative values are shown by dashed lines (using the same contour interval). Thin black contours are isentropes at a 1-K interval. Wind velocity vectors are overlaid as arrows.

as a useful complement to the linear theory, which performs best in the VE and ST regimes.

5. The nonlinear response

Although the linear scaling in (17) was successful at predicting W_t for the VE and ST flow regimes, it failed to accurately predict the updraft phase, strength, and sensitivity to a_m for the nonlinear GD regime. To gain insight into the mechanisms that control the circulations in this part of parameter space, we provide an in-depth analysis of the nonlinear numerical simulations, using

the linear solutions as a reference to expose the nonlinear effects.

a. Physical characteristics

Some essential differences between the linear and nonlinear flow responses are shown in Fig. 7, which compares w and b fields for the case with $h_m = 100$ m and $a_m = 5$ km (termed the "HM100-AM5" case) at 0600 and 1000 LT. At sunrise (0600 LT), the linear solution contains a strong downdraft at the terrain centerpoint surrounded by two updrafts (Fig. 7a), which is identical to the baseline case (Fig. 3a) except for a larger

magnitude. The numerical model also has a central downdraft at that time, but its magnitude falls below the minimum contour interval (Fig. 7b). These circulations are accompanied by radically different b signatures; whereas the linear model has a cold anomaly extending vertically through the boundary layer, the numerical model has a thin, surface-based cold layer spread over a broad area (Figs. 7c,d). In the latter, nocturnal cooling above the terrain leads to a downward plunging of cold air and the formation of two density currents that transport negatively buoyant air outward (not shown). Despite the very idealized nature of this experiment, this is a realistic effect that resembles katabatic winds or coastal land breezes (e.g., Mahrt 1982). Between 0600 and 1000 LT the boundary layer downdraft strengthens in the linear model as cold air persists over the terrain, reflecting the high thermal inertia of this case (Figs. 7e and g). By contrast, the numerically simulated downdraft transitions into a compact updraft over the terrain centerpoint, which coincides with a relatively narrow buoyancy anomaly (Figs. 7f and h). Again, the narrowness of this updraft is consistent with real thermal circulations, the central updrafts of which collapse into sharp zones of concentrated ascent (e.g., Kirshbaum 2011; Barthlott et al. 2011).

The sensitivity of the thermal circulations to a_m is illustrated by Fig. 8, which compares time series of relevant quantities for two cases in the nonlinear GD regime: the HM100-AM5 case (again, with $a_m = 5$ km) and the HM100-AM20 case (with $a_m = 20$ km). Four quantities are calculated within an analysis box covering $0 \leq [\tilde{x}, \tilde{z}] \leq 1$: (i) the averaged buoyancy b_{avg}, (ii) the minimum surface pressure p'_{min}, (iii) the maximum vertical velocity w_{max}, and (iv) the averaged horizontal vorticity η_{avg}. Both b_{avg} and p'_{min} are largely insensitive to a_m in the linear solutions, with the maximum of the former and minimum of the latter coinciding at around 1700 LT (Figs. 8a and c). By contrast, the numerical model solutions indicate a major phase shift between the two cases, with the maximum b_{avg} (and minimum p'_{min}) falling at around 1130 LT in the HM100-AM5 case and at around 1600 LT in the HM100-AM20 case (Figs. 8b and d). Moreover, the peak magnitudes of the simulated b_{avg} and p'_{min} are significantly lower in the HM100-AM5 case than in the corresponding linear solution or the HM100-AM20 case. The linear model predicts both circulations reaching their maxima at 2200 LST, with much larger w_{max} and η_{avg} for the HM100-AM5 case (Figs. 8e and g). By contrast, in the numerical solutions w_{max} and η_{avg} have similar peak magnitudes but differ mainly in phase (Figs. 8f and h).

b. Vorticity analysis

To conceptually explain the substantial differences between the linear and nonlinear responses in Figs. 7–8,

we examine the horizontal vorticity and the processes that control it. Taking the curl of the nonlinear Boussinesq momentum equation in (1) gives

$$\frac{\partial \eta}{\partial t} = -(\mathbf{v}' \cdot \mathbf{\nabla})\eta - \frac{\partial b}{\partial x} - \alpha \frac{\partial \eta}{\partial t} \qquad (23)$$

where we have set $\overline{U} = N_0 = 0$ for application to the GD regime. The first term on the right-hand side of (23) is the nonlinear vorticity advection, the second is the horizontal buoyancy gradient, and the third is damping. Although the simplified Boussinesq representation of η in (23) differs from that in the fully compressible numerical model, it still provides useful and straightforward insight into the behavior of the simulated flow.

Figure 9 provides a snapshot of the advection and buoyancy gradient terms of (23) during the growth phase of the HM100-AM5 simulation at 1000 LT (because the damping term cannot strengthen the circulation, we do not analyze it in detail). The buoyancy gradient term clearly increases (decreases) η for $x > 0$ ($x < 0$), which tends to strengthen the overall convective circulation (Fig. 9a). The advection terms have a more complex structure, with a strong couplet straddling $x = 0$ that locally sharpens the circulation and secondary features farther from the center (Fig. 9b). The broad evolution of these terms is shown by time series for the HM100-AM5 and HM100-AM20 cases in Fig. 10, which are again averaged over $0 \leq [\tilde{x}, \tilde{z}] \leq 1$. Whereas the buoyancy gradient monotonically increases the vorticity for several hours in both cases, the nonlinear advection generally tends to weaken it. Although the couplet at $x = 0$ in Fig. 9b amplifies the vorticity locally, it evidently does not strengthen the overall mountain-scale solenoidal circulation because of cancellations with other features within the analysis box. Thus, the buoyancy gradient term drives the overall circulation, with the nonlinear advection acting primarily to tighten the central updraft into a narrow core.

The main sensitivity to a_m in Fig. 10 is that $|\partial b/\partial x|$ initially increases faster but reaches its apex much earlier in the HM100-AM5 case (around 1000 LT) than in the HM100-AM20 case, where it slowly increases to a maximum at around 1430 LT. Because the buoyancy gradient driving the latter circulation is maintained for substantially longer, the circulation ultimately becomes more vigorous. This is consistent with the evolution of the four quantities in Fig. 8. Whereas the magnitude of each quantity initially grows faster in the HM100-AM5 case, it eventually becomes larger in the HM100-AM20 case owing to its extended growth phase. In addition,
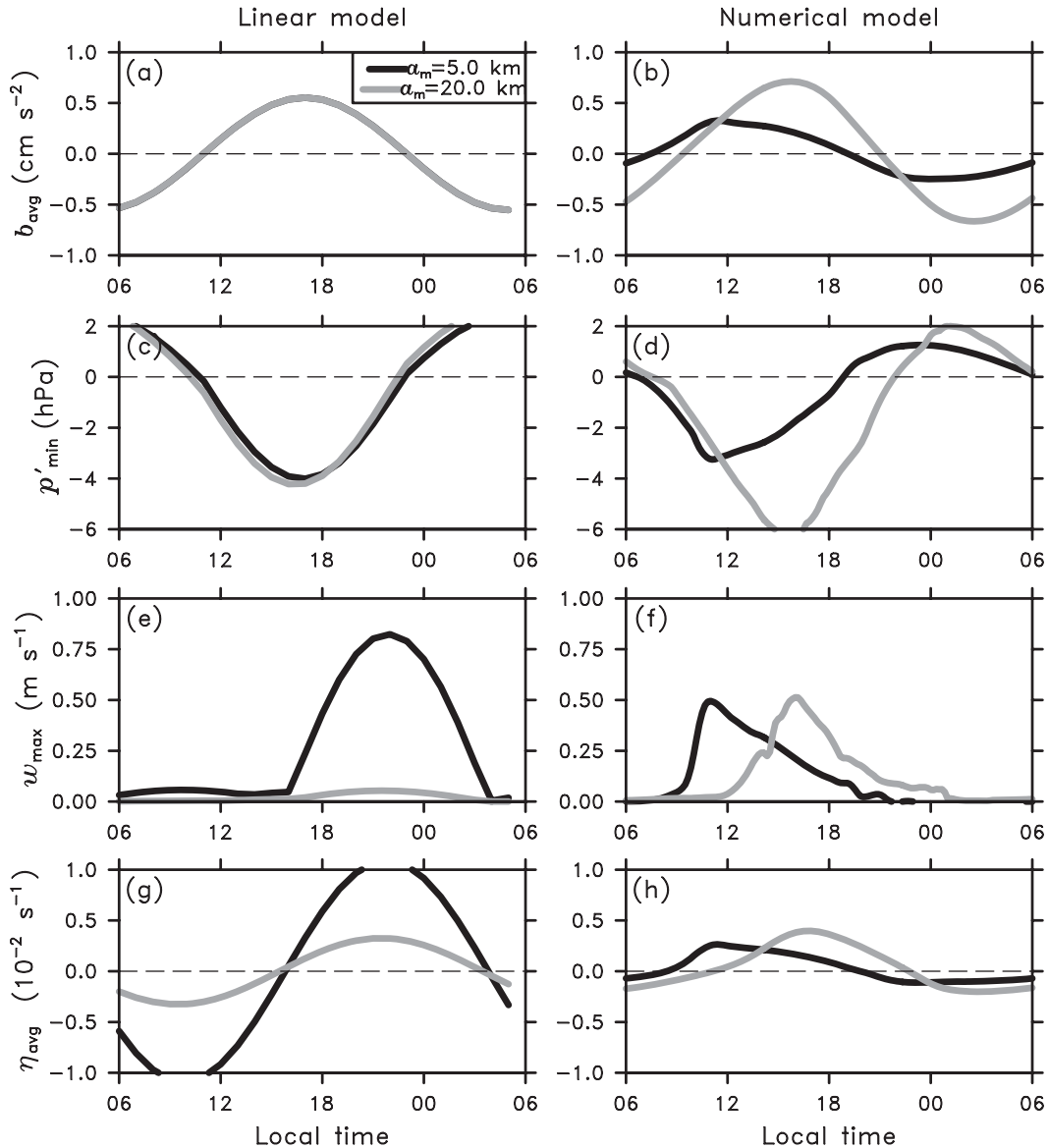
FIG. 8. Time series of various quantities, calculated over the region $0 \le [\tilde{x}, \tilde{z}] \le 1$ for the HM100-AM5 (black lines) and HM100-AM20 (gray lines) cases from the (left) linear and (right) numerical models: (a),(b) mean buoyancy, (c),(d) minimum pressure, (e),(f) maximum vertical velocity, and (g),(h) averaged vorticity.

Fig. 10b indicates that nonlinear momentum advection substantially weakens the circulation in the HM100-AM5 case between 1000 and 1800 LT (Fig. 10b). A similar trend is apparent in the HM100-AM20 case over 1400–2100 LT, but with a significantly lower amplitude.

Given the central importance of the horizontal buoyancy gradient for driving the circulation, one must understand the factors that control it to interpret the behavior of thermally forced flows. To this end, we analyze the time derivative of $-\partial b/\partial x$, which is given by

$$\frac{\partial}{\partial t}\left(-\frac{\partial b}{\partial x}\right) = -\frac{\partial}{\partial x}\left(\frac{\partial b}{\partial t}\right) = \frac{\partial}{\partial x}\left(u\frac{\partial b}{\partial x}\right) + \frac{\partial}{\partial x}\left(w\frac{\partial b}{\partial z}\right)$$
$$- \frac{\partial Q}{\partial x} + \alpha\frac{\partial b}{\partial x}. \tag{24}$$

The first two terms on the right-hand side are related to the nonlinear buoyancy advection, the third is the horizontal gradient of the heating function, and the fourth is damping. The evolution of the first three terms (again averaged over $0 \le [\tilde{x}, \tilde{z}] \le 1$) is compared for the
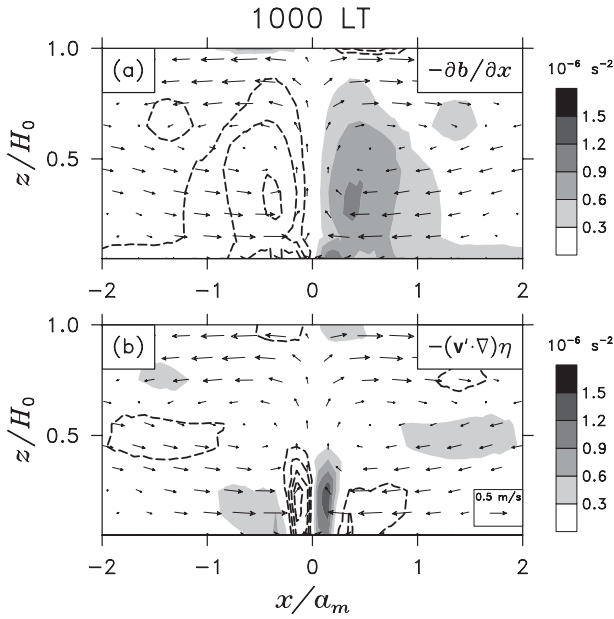
FIG. 9. Illustration of the dominant terms contributing to the averaged vorticity tendency in (23), for the HM100-AM5 simulation at 1000 LT: (a) the negative horizontal buoyancy gradient and (b) the nonlinear advection. Positive values are shown by filled grayscale contours and negative values are shown by dashed lines (with the same contour interval). Wind velocity vectors are overlaid as arrows.
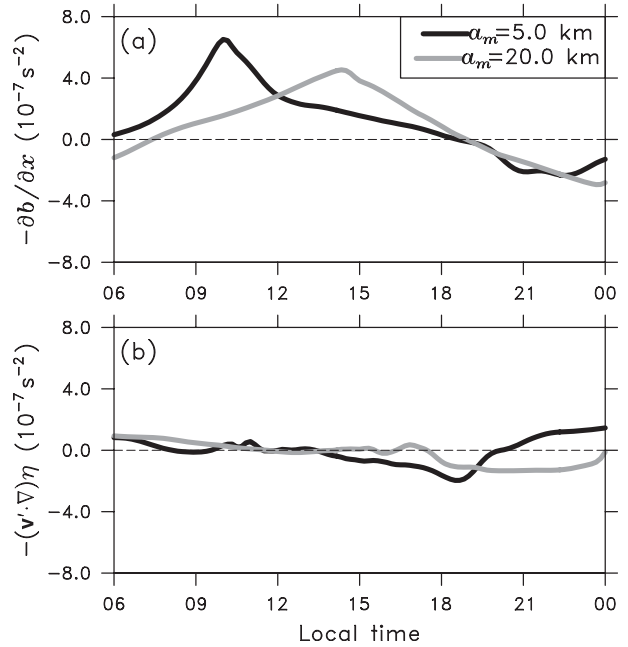

FIG. 10. Time series of the dominant terms contributing to the averaged vorticity tendency in (23), for the HM100-AM5 (black lines) and HM100-AM20 (gray lines) simulations: (a) the negative horizontal buoyancy gradient and (b) the nonlinear advection. These quantities are calculated over $0 \leq [\tilde{x}, \tilde{z}] \leq 1$.

HM100-AM5 and HM100-AM20 cases in Fig. 11. As the convective circulations gain strength under diurnal heating, the horizontal advection term $(u \partial b/\partial x)_x$ transitions from positive to negative (Fig. 11a). Henceforth, this term possesses the same sign as, and attains similar magnitudes to, the diurnal heating term $(-\partial Q/\partial x)$ (Fig. 11c). It enhances the horizontal buoyancy gradients by squeezing b contours together, which is reflected by the b evolution over 0930–1230 LT in Fig. 12. From 0930 to 1030 LT the main buoyancy anomaly transitions from a cone into a mushroom shape, with a relatively narrow central core (Figs. 12a,b and Fig. 7h). The associated increase in $|\partial b/\partial x|$ forces $|\eta_{avg}|$ to increase, which, in turn, contracts the anomaly further. This positive feedback continues until the vertical advection term $(w \partial b/\partial z)_x$ sharply increases to oppose further growth of the circulation (Fig. 11b).

The emergence of the vertical buoyancy advection term occurs earlier (1000 LT) in the HM100-AM5 case than in the HM100-AM20 case (1430 LT) because its stronger initial buoyancy gradients promote faster development of the circulation. At this time, a sharp increase in heat ventilation by the main updraft core transports the warmest air from the surface to the upper boundary layer (Figs. 12b,c). This air then spreads laterally, entrains free-tropospheric air to warm further,

and begins to subside within the convective downdrafts. A large thermal anomaly is apparent by 1230 LT with two broad, symmetric lobes centered at $\tilde{x} = \pm 1.5$ (Fig. 12d). With the buoyancy spread over a relatively large area, the overall convective circulation undergoes a broadening and weakening, which is reflected by the slow decrease in η_{avg} and w_{max} from 1100 to 1800 LT in Figs. 8f and h. The same process occurs in the HM100-AM20 case after 1430 LT case, once the circulation is sufficiently strong for vertical momentum advection to displace the main surface-based buoyancy anomaly.

6. Conclusions

We have applied simple theoretical models and nonlinear numerical simulations to study the dynamics of thermally driven circulations forced by spatial gradients in terrain height and/or surface heating. A two-layer linear model, and an accompanying scaling of the linearized equations, was used to predict the strength of these circulations for a broad range of background flows, terrain geometries, and surface heating rates. For simplicity this model uses a steady background flow and neglects the Coriolis force, which renders it most applicable to synoptically quiescent, high-Rossby-number flow in the tropics or over meso-γ-scale midlatitude
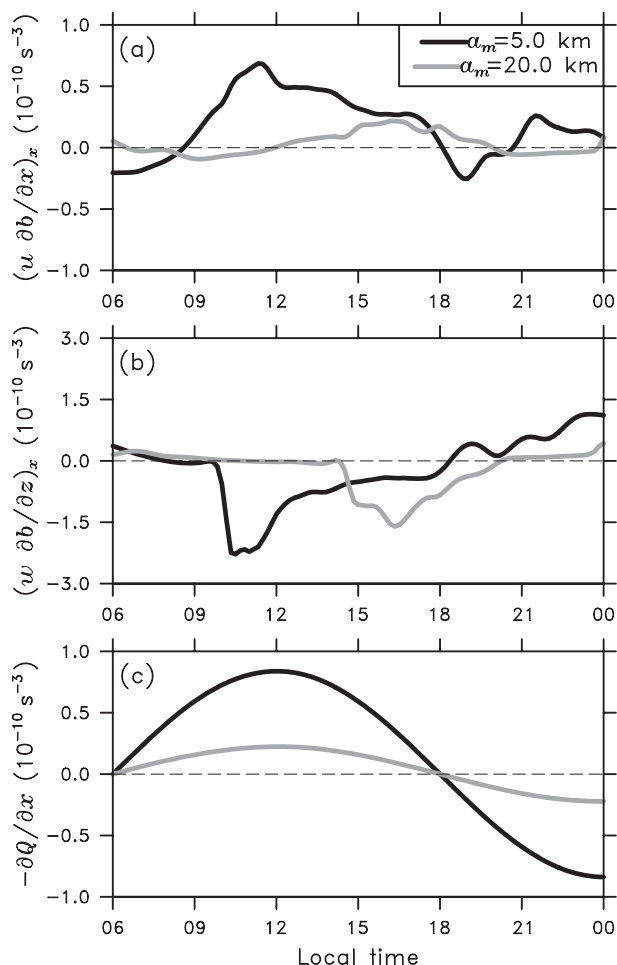
FIG. 11. Time series of the dominant terms contributing to the $-\partial b/\partial x$ tendency in (24), for the HM100-AM5 (black lines) and HM100-AM20 (gray lines) simulations: (a) the zonal buoyancy advection, (b) the vertical buoyancy advection, and (c) the horizontal gradient of the heating function Q. These quantities are calculated over $0 \le [\tilde{x}, \tilde{z}] \le 1$.

features. Although highly idealized, this model represents an advancement in the study of terrain-forced circulations because of its inclusion of time variability and multilayer stability profiles, which admit important realistic effects. Focus was placed on the strength of the updraft branches of the circulations, which often give rise to meteorologically significant phenomena. The linear scalings were compared to those obtained from a separate thermodynamic heat-engine scaling and to simulations with a nonlinear and fully compressible numerical model.

In addition to quantifying the bounds of applicability of linear theory and the relative strength of thermal versus mechanical circulations, the linear scaling was used to separate heated-terrain flows into three regimes.

These regimes correspond to the following scenarios: (i) convective boundary layers under weak winds (the "growth–decay" regime), (ii) convective boundary layers under moderate to strong winds (the "ventilation" regime), and (iii) stable boundary layers (the "stratification" regime). Predictions from the linear scaling were highly accurate in regimes (ii)–(iii) for all of the flows considered. However, they failed in regime (i) for cases with realistic forcing amplitudes. In that regime, the heat-engine scaling significantly outperformed the linear model.

In the growth–decay regime, a solenoidal circulation developed with an intense updraft directly over the terrain centerpoint surrounded by two symmetric downdrafts. Compared to the other two regimes, updrafts in this regime were by far the strongest (by multiple orders of magnitude), suggesting that convective boundary layers with weak winds provide the strongest thermal forcing for convection initiation (all other things being equal). The highly nonlinear dynamics in this regime acted to contract the central updraft and buoyancy anomaly into a narrow core, which amplified the circulation by strengthening the thermal gradients that drive it. The nonlinearities then diminished the growth of the circulation by ventilating the warmest surface-based air to the upper boundary layer, where it spread outward to distribute the heating over a large area. This rapid contraction of boundary layer horizontal convergence zones to a critical intensity, followed by a slow weakening, is likely a general feature of thermal circulations over differentially heated surfaces (and not restricted to mountain flows).

In the ventilation regime, the updrafts weakened rapidly with increasing background winds because of the inability of buoyancy to accumulate over the terrain. The strongest afternoon updraft formed downwind of the heat source, with subsidence upwind and directly over the hill (in agreement with CT05). In this regime, afternoon convection initiation is thus more likely to form downwind of the high terrain, which is consistent with recent observations from the Convective and Orographically Induced Precipitation Study (COPS) field project (Hagen et al. 2011). The stratification regime was dominated by vertically propagating gravity waves initiated as a thermally direct response to the localized heating. Under zero background winds, a plume of decaying ascent developed over the heat source, surrounded by tilted beams of descent. In the presence of background winds, the waves tilted upstream against the mean flow, reminiscent of the steady-state solutions obtained by CT05. Of the three regimes, the updrafts were the weakest in the stratification regime because of the effectiveness of vertical motion at
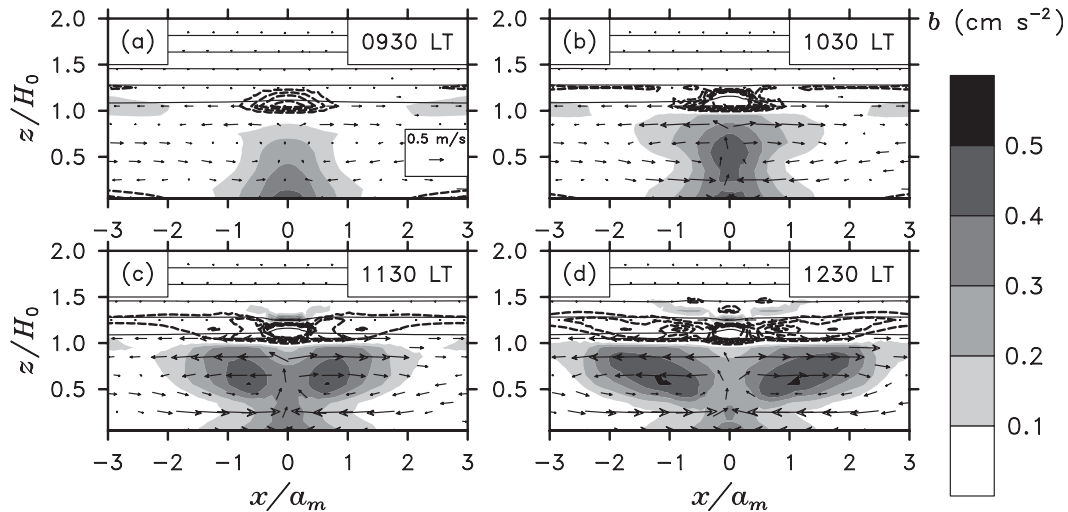
FIG. 12. Evolution of the convective circulation and central buoyancy anomaly in the HM100-AM5 case, in hourly intervals: (a) 0930, (b) 1030, (c) 1130, and (d) 1230 LT. Positive values of b are shown by filled grayscale contours and negative values by dashed lines (with the same contour interval). Velocity vectors shown by arrows, all using the same reference scale as that shown in (a).

diminishing the central buoyancy anomaly, along with the gravity wave transport of perturbation energy away from the heat source.

The success of the linear and heat-engine scalings offers some hope for improved parameterization of related processes (e.g., convection initiation, aerosol venting) in large-scale models. However, the very idealized nature of this analysis, which helped to isolate the key processes of interest, may also compromise the real-world applicability of these results. For one thing, the linear scaling is only strictly applicable to very short hills; degradation of the linear solutions was apparent for even modestly sized (100 m) hills. The fundamental nonlinearity of thermally forced terrain circulations over larger obstacles thus diminishes the predictive skill of the linear scaling. Moreover, although the scaling provided insights into the relative importance of mechanical versus thermal forcing, the mechanical response was never explicitly evaluated. In the linear limit, the thermal and mechanical responses formally decouple and may simply be summed together (CT05). However, for nonlinear flows significant interactions may occur between these responses that were not addressed herein. These interactions remain an important yet poorly understood topic in need of attention. Finally, other than including dissipative terms in our linear and numerical models, we did not explicitly consider the impacts of turbulence on the thermal circulations. This likely resulted in an underestimation of boundary layer mixing and entrainment of free-tropospheric air. Because this mixing effectively

diminishes the horizontal buoyancy gradients driving the thermal circulations, the strength of these circulations may have been significantly overestimated. Taken together, these limitations demand that additional research using three-dimensional large-eddy simulation be undertaken to more realistically represent the complex interactions between thermal circulations, mechanical forcing, and turbulent processes over heated terrain.

APPENDIX

Solving the Two-Layer System

The general solutions to the ordinary differential equation in (11) for layers 0 and 1 may be written

$$\hat{w}_0 = A_0 e^{im_0 z} + B_0 e^{-im_0 z} + \frac{k^2 \hat{q}}{\sigma^2 (m_1^2 + D^{-2})} e^{-z/D}, \quad \text{(A1)}$$

$$\hat{w}_1 = A_1 e^{im_1 z} + B_1 e^{-im_1 z} + \frac{k^2 \hat{q}}{\sigma^2(m_1^2 + D^{-2})} e^{-z/D}, \quad \text{(A2)}$$

where A_0, B_0, A_1, and B_1 are unknown complex coefficients determined by application of four boundary conditions, and m_0 and m_1 are chosen to be the positive roots of m_0^2 and m_1^2. The boundary conditions include (i) the linearized free-slip lower boundary condition $\hat{w}_1|_{z=0} = \overline{U}\partial h/\partial x$, which, when substituted into (A1), gives

$$A_0 + B_0 = i\overline{U}k\hat{h} - \frac{k^2\hat{q}}{\sigma^2(m_1^2 + D^{-1})}; \quad \text{(A3)}$$

(ii) the upper radiation condition, which enforces upward energy flux in layer 1; and the matching of (iii) the displacement and (iv) pressure at the $z = H_0$ interface. The upper radiation condition is satisfied if the horizontally averaged vertical energy flux $\overline{Pw}$ is positive. To mathematically represent this condition, we follow Durran (1990) by deriving the polarization relations between P and w separately for two normal modes of the form $w_a = \text{Re}[A_1 e^{-i(kx+mz-\omega t)}]$ and $w_b = \text{Re}[B_1 e^{-i(kx-mz-\omega t)}]$. Substituting these expressions into (4)–(7) yields

$$p_a = \frac{m\sigma}{k^2} w_a, \quad \text{(A4)}$$

$$P_b = -\frac{m\sigma}{k^2} w_b. \quad \text{(A5)}$$

For $m_1^2 > 0$ and $\text{Re}(m) > 0$, the solution consists of vertically propagating gravity waves. In this case, the sign of $\overline{P_a w_a} > 0$ is the same as that of $\text{Re}(\sigma)$. We thus set $B_1 = 0$ for $\text{Re}(\sigma) > 0$ and $A_1 = 0$ for $\text{Re}(\sigma) < 0$. This is implemented by retaining A_1 and replacing its exponential argument with iSm_2, where $S = \text{sign}[\text{Re}(\sigma)]$. For $m_1^2 < 0$, the two terms in (A2) respectively correspond to exponentially growing and decaying modes. To enforce a bounded solution we thus eliminate B_2 in that case.

Finally, the matching conditions at the interface $z = H_0$ are applied. For a uniform background wind the displacement and pressure matching conditions are equivalent to matching $\hat{w}$ and $\partial\hat{w}/\partial z$:

$$A_0 e^{im_1 H_0} + B_0 e^{-im_1 H_0} - A_1 e^{iSm_2 H_0}$$
$$= \frac{k^2\hat{q}(m_2^2 - m_1^2)e^{-H_0/D}}{\sigma^2(m_1^2 + D^{-2})(m_2^2 + D^{-2})}, \quad \text{(A6)}$$

$$im_1(A_0 e^{im_1 H_0} - B_0 e^{-im_1 H_0}) - iSm_2 A_1 e^{-iSm_2 H_0}$$
$$= -\frac{k^2\hat{q}(m_2^2 - m_1^2)e^{-H_0/D}}{\sigma^2 D(m_1^2 + D^{-2})(m_2^2 + D^{-2})}. \quad \text{(A7)}$$

Equations (A3), (A6), and (A7) constitute a linear system of three equations and three unknowns. They are solved analytically to give closed-form expressions for $\hat{w}_1$ and $\hat{w}_2$ for each mode of the discrete Fourier decomposition (not shown). The resulting arrays of Fourier coefficients are then inverse transformed and the real part is retained to give w_1 and w_2 in physical space. The forward and inverse discrete Fourier transforms are performed in MATLAB using their FFT and IFFT functions. Note that the potential singularity associated with $\sigma = 0$ is avoided by choosing a nonzero α.

REFERENCES

Banta, R. M., 1990: *Atmospheric Processes over Complex Terrain.* Meteor. Monogr., No. 45, Amer. Meteor. Soc., 323 pp.

Barthlott, C., and Coauthors, 2011: Initiation of deep convection at marginal instability in an ensemble of mesoscale models: A case study from COPS. *Quart. J. Roy. Meteor. Soc.,* **137,** 118–136.

Bryan, G. H., and J. M. Fritsch, 2002: A benchmark simulation for moist nonhydrostatic models. *Mon. Wea. Rev.,* **130,** 2917–2928.

Crook, N. A., and D. F. Tucker, 2005: Flow over heated terrain. Part I: Linear theory and idealized numerical simulations. *Mon. Wea. Rev.,* **133,** 2552–2564.

Defant, F., 1952: Local winds. *Compendium of Meteorology,* T. F. Malone, Ed., Amer. Meteor. Soc., 655–672.

Durran, D. R., 1990: Mountain waves and downslope winds. *Atmospheric Processes over Complex Terrain, Meteor. Monogr.,* No. 45, Amer. Meteor. Soc., 59–83.

Hagen, M., J. van Baelen, and E. Richard, 2011: Influence of the wind profile on the initiation of convection in mountainous terrain. *Quart. J. Roy. Meteor. Soc.,* **137,** 224–235.

Haiden, T., 2003: On the pressure field in the slope wind layer. *J. Atmos. Sci.,* **60,** 1632–1635.

Jiang, Q., 2012a: A linear theory of three-dimensional land–sea breezes. *J. Atmos. Sci.,* **69,** 1890–1909.

——, 2012b: On offshore propagating diurnal waves. *J. Atmos. Sci.,* **69,** 1562–1580.

Jury, M. R., and S. Chiao, 2011: Mesocirculation associated with summer convection over the central Antilles. *Earth Interact.,* **15,** 1–19.

Kirshbaum, D. J., 2011: Cloud-resolving simulations of deep convection over a heated mountain. *J. Atmos. Sci.,* **68,** 361–378.

Mahrt, L., 1982: Momentum balance of gravity flows. *J. Atmos. Sci.,* **39,** 2701–2711.

Qian, T., C. C. Epifanio, and F. Zhang, 2009: Linear theory calculations for the sea breeze in a background wind: The equatorial case. *J. Atmos. Sci.,* **66,** 1749–1763.

Reisner, J. M., and P. K. Smolarkiewicz, 1994: Thermally forced low Froude number flow past three-dimensional obstacles. *J. Atmos. Sci.,* **51,** 117–133.

Renno, N. O., and A. P. Ingersoll, 1996: Natural convection as a heat engine: A theory for CAPE. *J. Atmos. Sci.,* **53,** 572–585.

Robinson, F. J., S. C. Sherwood, and Y. Li, 2008: Resonant response of deep convection to surface hot spots. *J. Atmos. Sci.,* **65,** 276–286.

Rotunno, R., 1983: On the linear theory of the land and sea breeze. *J. Atmos. Sci.,* **40,** 1999–2009.

Smith, R. B., and Y.-L. Lin, 1982: The addition of heat to a stratified airstream with application to the dynamics of orographic rain. *Quart. J. Roy. Meteor. Soc.,* **108,** 353–378.

Souza, E. P., N. O. Renno, and M. A. F. S. Dias, 2000: Convective circulations induced by surface heterogeneities. *J. Atmos. Sci.,* **57,** 2915–2922.

Stevens, B., J. Duan, J. C. McWilliams, M. Münnich, and J. D. Neelin, 2002: Entrainment, Rayleigh friction, and boundary layer winds over the tropical pacific. *J. Climate,* **15,** 30–54.

Tian, W. S., and D. J. Parker, 2003: A modeling study and scaling analysis of orographic effects on boundary layer shallow convection. *J. Atmos. Sci.,* **60,** 1981–1991.